Optics & Laser Technology 203 (2026) 115706

Contents lists available at ScienceDirect

Optics and Laser Technology

journal homepage: www.elsevier.com/locate/optlastec

Full length article

All-optical optical-acoustic fusion technology: A novel method for defect detection and 3D reconstruction in PCBs

Jianghao Zhao [a,b], Fei Wang [a,b,*], Peng Yin [a,b], Zhuoyan Yue [a,b], Feng Yang [a,b], Honghao Yue [a,b], Stefano Sfarra [d], Lixia Xu [c], Xiaqiao Li [c], Dongkangkang Chen [c], Junyan Liu [a,b,*]

[a] National Key Laboratory of Aerospace Mechanism, Harbin, Heilongjiang 150000, China
[b] School of Mechatronics Engineering, Harbin Institute of Technology, Harbin 150001, China
[c] Beijing Satellite Manufacturing Factory Co. LTD, Beijing 100001, China
[d] Department of Industrial and Information Engineering and Economics, University of L'Aquila, 67100, Italy

ARTICLE INFO

Keywords:
Optical-acoustic fusion
Defect detection
3D reconstruction
LUT
PCBs

ABSTRACT

Laser ultrasonic testing (LUT) offers high-resolution, non-contact and material-flexible detection. However, its point-by-point scanning mode limits efficiency, making it well-suited for detailed evaluation of critical regions while posing challenges for automated defect positioning and detection. To address this limitation, this study proposed an optical image-based positioning method, which integrated optical imaging and LUT for automated defect detection and 3D reconstruction in printed circuit boards (PCBs). Optical images are used for locating the detection region and guiding LUT scanning, and LUT results are fused with optical images to achieve intuitive defect visualization. An acoustic attenuation–based model is used for defect depth estimation, yielding an average error of 5.56 % in the detection region. Experimental results demonstrate that the proposed method accurately reveals both surface morphology and subsurface defect features. Quantitative comparison with infrared thermography (IR) shows that LUT provides higher imaging quality and improved depth-to-diameter detectability for subsurface defects. The fusion image achieves a positioning error of approximately 0.32 mm and an average IoU of approximately 0.643, demonstrating the feasibility of the system for 3D visualization.

1. Introduction

During the manufacturing and operation of printed circuit boards (PCBs), subsurface defects such as delamination and cracking are prone to occur due to alternating thermal and mechanical stresses, seriously affecting the reliability of electronic devices [1]. Therefore, high-precision defect detection is essential to ensure the quality of PCBs.

Various non-destructive testing (NDT) methods have been explored for PCB defect inspection, each exhibiting distinct advantages and limitations. Optical imaging is widely used for surface defect detection in PCBs [2]; however, it is limited to surface features and cannot reveal hidden subsurface defects. Infrared thermography (IR) is also a commonly employed NDT method due to its efficiency [3,4,5], although its resolution is limited for small or deep defects. Ultrasound-based techniques are widely used for subsurface defect detection due to their high sensitivity [6]. Conventional ultrasonic testing (UT) typically employs piezoelectric transducers, which require couplants to match the acoustic impedance at the air–solid interface [7]. Scanning acoustic microscopy (SAM) provides very high-resolution, non-destructive imaging of subsurface defects, but usually requires a liquid coupling medium such as deionized water [8,9]. Terahertz imaging offers high-resolution, non-contact detection, but its efficiency is low, the cost is high, and it cannot penetrate metal materials [10]. Laser ultrasonic testing (LUT) directly induces ultrasonic waves in the material without couplants, enabling fully non-contact detection, and has been widely applied in defect detection [11,12,13,14,15]. The advantages and limitations of these detection methods are summarized in Table 1.

While each method has own characteristic, LUT stands out for its fully non-contact operation and high resolution. However, its point-by-point scanning mechanism makes it difficult to automatically locate scanning regions. Recent advances in robot-assisted NDT have shown that optical sensing can enhance detection automation. However, existing methods primarily rely on 3D scan data or predefined CAD models for path planning [16,17], making it difficult to achieve precise

* Corresponding authorsat: School of Mechatronics Engineering, Harbin Institute of Technology, Nangang District Xidazhi Street 92#, 150001, Harbin, Heilongjiang province, PR China.
E-mail addresses: wangfeipublic@hit.edu.cn (F. Wang), ljywlj@hit.edu.cn (J. Liu).

https://doi.org/10.1016/j.optlastec.2026.115706
Received 2 March 2026; Received in revised form 13 May 2026; Accepted 5 June 2026
Available online 11 June 2026
0030-3992/© 2026 Published by Elsevier Ltd.

Table 1
The advantages and limitations of various detection methods.

Method	Advantages	Main limitations
Optical	High efficiency; high resolution.	Cannot detect subsurface defects.
UT	High sensitivity and resolution; widely used; low cost.	Requires couplants; contaminate material.
X-ray CT	Highly sensitive; provides intuitive imaging results.	Radiation pollution; unsuitable for in-service or on-site detection.
SAM	Very high-resolution; non-destructive.	Typically requires a liquid coupling medium.
IR	Non-contact; high efficiency; widely used.	Limited detection depth; low spatial resolution.
Terahertz	Non-contact; high-resolution.	Low efficiency; high cost; cannot penetrate metals.
LUT	Non-contact; high sensitivity and spatial resolution; applicable to various materials.	Low efficiency; difficult to locate, non-intuitive results.

target detection region positioning based on real-time optical imaging. In the context of LUT, existing robotized studies also adopt similar 3D model path generation strategies [18,19] and fail to utilize real-time optical images for target region positioning and guidance. Prior hybrid methods, which combine optical imaging with acoustic sensing for non-destructive evaluation, have demonstrated improved defect characterization capability through complementary sensing mechanisms [20,21,22,23,24]. However, these approaches typically focus on data-level fusion of independently captured images, and do not address the challenge of using optical information to actively guide the LUT scanning process and locate target regions. To address these limitations, this study proposes an optical image-guided, all-optical optical-acoustic fusion detection method that enables automatic scanning region positioning, optical-acoustic fusion imaging, and three-dimensional (3D) defect reconstruction.

Recent advances in deep learning have significantly promoted multimodal data fusion for NDT applications [25,26,27]. However, these data-driven fusion approaches are primarily trained for specific materials, requiring extensive labeled datasets and exhibiting limited generalization to variations in materials and geometries. In contrast, this study employs a physics-driven fusion strategy such as Poisson fusion, which is training-free, and more robust for optical-acoustic image integration under limited data conditions.

Regarding ultrasonic sensing, conventional piezoelectric sensors require couplants, may risk damaging the specimen surface, and have limited bandwidth [28]. Laser interferometers provide non-contact measurements of surface vibration but require high surface smoothness [29], which is not suitable on PCBs with scratches or irregular textures. In contrast, all-optical ultrasonic sensors based on Fabry Perot (F-P) resonators provide non-contact, high-sensitivity measurements [30,31,32], making them well-suited for high-resolution ultrasonic detection in PCBs. The concise workflow is as follows: calibration → target region selection → coordinate mapping → LUT → fusion/ 3D reconstruction.

The main contributions of this study are summarized as follows.

1) An automated optical image–guided LUT method is proposed, achieving fully automated LUT of any regions through coordinate transformation, and addressing the limitations of manual alignment and spatial registration in conventional LUT.

2) An optical-acoustic fusion imaging system is developed, achieving simultaneous visualization of surface morphology and subsurface defect features, and addressing the limitations of non-intuitive results in single-modal detection.

3) An attenuation-based defect depth estimation method is proposed, achieving quantitative defect depth estimation and 3D reconstruction, and providing a solution for defect depth quantization problem of LUT.

The proposed method is not intended to extend the minimum detectable defect size beyond conventional LUT, but rather to enhance the automation, positioning efficiency, and multimodal visualization capabilities.

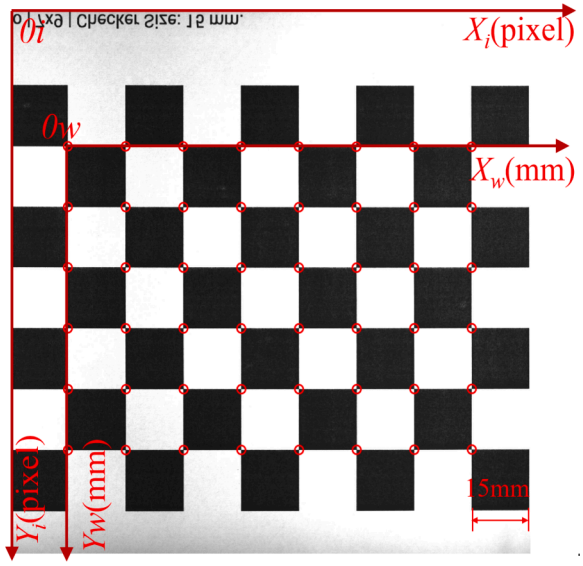


Fig. 1. Chessboard calibration image captured by the camera in its predefined working pose, and the definitions of the image and world coordinate systems.

The remainder of this paper is organized as follows. Section 2 presents an analysis model of laser-induced ultrasonic and provides a detailed introduction to the optical image-based positioning method. Section 3 introduces the manufacturing of PCB specimens with artificial defects and the development of an automated all-optical optical-acoustic fusion detection system. Section 4 details the experimental verification of the developed system. Finally, Section 5 concludes the paper and discusses future works.

2. Theoretical background

2.1. Principle of laser-induced ultrasonic

Laser-induced ultrasonic in this study is based on the thermoelastic effect. When a pulsed laser irradiates the material surface, the absorbed optical energy induces transient thermal expansion, thereby generating broadband ultrasonic waves in the specimen. Subsurface defects perturb ultrasonic propagation characteristics, resulting in measurable variations in signal amplitude and waveform features. The transient temperature field induced by pulsed laser excitation is expressed by the heat conduction equation:

$$\rho c \frac{\partial T}{\partial t} = \nabla \cdot (k \nabla T) + Q \tag{1}$$

where c is the specific heat capacity, ρ is the material density, k is the thermal conductivity, T is the temperature field in the material, and Q is the heat source energy density induced by pulsed laser excitation. The thermoelastic response further generates elastic displacement waves in the material, which can be described as:

$$\rho \frac{\partial^2 \boldsymbol{U}}{\partial t^2} = (\lambda + \mu) \nabla (\nabla \cdot \boldsymbol{U}) + \mu \nabla^2 \boldsymbol{U} - \alpha (3\lambda + 2\mu) \nabla T \tag{2}$$

where λ and μ are the Lamé constants of the material, α is the thermal expansion coefficient, and $\boldsymbol{U}$ is the displacement field. Subsurface defects introduce discontinuities in acoustic impedance and wave propagation paths, thereby altering the ultrasonic response. By analyzing the acquired ultrasonic signals, defect information can be extracted for subsurface defect imaging and characterization.

2.2. Method of optical image-based positioning

To achieve automated positioning of the LUT scanning region, an optical-guided coordinate mapping framework was established in this study. Optical images acquired by the camera serve as the spatial reference for determining the position of the target detection region and guiding the robotic motion of the detection module. The relationship between the world coordinate system and the image coordinate system is expressed as:

$$\boldsymbol{P}_{\text{image}} = \boldsymbol{K}\cdot[\boldsymbol{R}|\boldsymbol{t}]\cdot\boldsymbol{P}_{\text{world}} \tag{3}$$

where $\boldsymbol{K}$ is the intrinsic matrix of the camera, and $[\boldsymbol{R}|\boldsymbol{t}]$ represents the extrinsic matrix describing the spatial relationship between the camera and the world coordinate system.

Zhang' calibration and PnP pose estimation methods were employed to estimate the intrinsic and extrinsic parameters of the camera system [33], the standard chessboard calibration plate is shown in Fig. 1. Since the camera and the detection module are rigidly fixed, the positioning relationship between them remains constant after calibration. Therefore, once the calibration is completed in the predefined working pose, the coordinate transformation can be reused for subsequent inspections without repeated recalibration.

During detection, the operator selects the target detection region directly on the optical image through the graphical user interface. The selected target detection region is then projected into the world coordinate system through the established coordinate transformation model. Based on the calculated spatial coordinates, the robotic arm automatically drives the detection module to the corresponding scanning region for LUT inspection. After LUT acquisition, the ultrasonic imaging results are spatially registered with the optical image according to the established coordinate mapping relationship. The registered data are subsequently used for optical-acoustic fusion imaging and defect visualization.

2.3. Discussion on calibration board configuration

For a fixed camera field of view, the choice of chessboard square size directly affects camera calibration accuracy, which directly affects the precision of the coordinate transformation between the image and world coordinate systems. If the square size is too small, individual squares occupy insufficient pixel area in the image, increasing the uncertainty of corner pixel coordinate extraction. Conversely, if the square size is too large, the number of detectable corners within the field of view decreases significantly, reducing the spatial sampling density and preventing the calibration algorithm from obtaining sufficient constraints, thereby also degrading coordinate transformation accuracy.

In this study, the selected 15 mm square size achieves a balance between corner positioning accuracy and spatial sampling density. Under this configuration, each calibration square occupies approximately 200 pixels in the image, ensuring reliable corner extraction and stable estimation of the intrinsic and extrinsic parameters. The defect positioning results presented in Section 4.3 experimentally validate the resulting positioning accuracy: the overall RMS positioning error is only 0.32 mm, indicating that the selected calibration configuration meets the positioning requirements. The residual positioning errors are primarily attributed to the repeatability of the robotic arm, the uncertainty in manual target detection area selection, and measurement errors in the rigid structure dimensions of the system.

3. 3.Materials and methods

3.1. Specimen

The specimen used in this study is a single-layer PCB made of glass fiber reinforced epoxy resin (FR4), the overall dimensions of the specimen are 120 mm × 100 mm × 3.2 mm. Artificial defects of different sizes and depths were pre-fabricated on the back of the specimen. As shown in Fig. 2. This study focuses on method validation rather than detailed actual defect detection, so artificially fabricated blind holes were used as reference defects in this study.

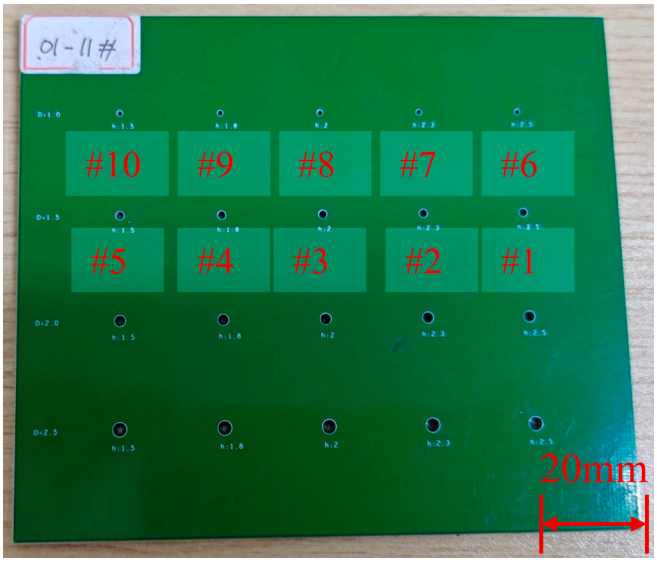


Fig. 2. Test specimen with artificial defects for method validation.

This study focuses on the detection of small defects, which are typically more challenging to identify. The target detection region includes 10 artificial defects, labeled as #1 to #10. The detailed geometric parameters (diameter and depth) of these defects are listed in Table 2.

All defects are flat bottomed holes, designed to simulate common subsurface defect types in PCBs, thereby providing a foundation for evaluating the performance of the detection system. Artificially fabricated holes are commonly used as controlled reference defects in LUT studies. The reasons are as follows:

(1) Their geometry, depth, and diameter can be precisely controlled, which is essential for quantitative validation of defect positioning accuracy, depth estimation error, and imaging SNR.

(2) The ultrasonic response to a sudden change in material properties at an air–solid interface, which is a key characteristic of real PCB defects. Therefore, although holes represent a simplified defect model, they capture the essential physical mechanism.

Nevertheless, we acknowledge that real PCB defects may exhibit more complex ultrasonic responses due to anisotropy, multilayer coupling. These factors may affect detection sensitivity and will require further investigation in future work.

3.2. Experimental setup

An automated all-optical optical-acoustic fusion detection system was developed in this study, as shown in Fig. 3, the proposed system consists of 2 main modules: (a) detection module and (b) robotic arm.

AUBO-i10 six degree of freedom (6-DOF) robotic arm is used as the motion platform. This robotic arm supports a maximum payload of 10 kg, with a repeatability of ± 0.03 mm and a maximum working radius of 1350 mm, ensuring high precision and stability.

The integrated detection module (Fig. 3(a).) installed at the end of the robot arm is shown in Fig. 4, which combines a LUT detection system and a high-resolution optical imaging system. The main components are as follows:

(a) F-P acoustic sensor. A F-P acoustic sensor (model Xarion Eta450 Ultra) with a frequency response from 50 kHz to 2 MHz and a sensitivity of 100 mV/Pa (@1 kHz, 0 dB gain, 50 Ω), enabling high-sensitivity, non-contact ultrasonic detection.

Table 2
Geometric parameters of defects #1 to #10.

Label	#1	#2	#3	#4	#5	#6	#7	#8	#9	#10
Diameter (mm)	1.5	1.5	1.5	1.5	1.5	1.0	1.0	1.0	1.0	1.0
Depth (mm)	0.7	0.9	1.2	1.4	1.7	0.7	0.9	1.2	1.4	1.7

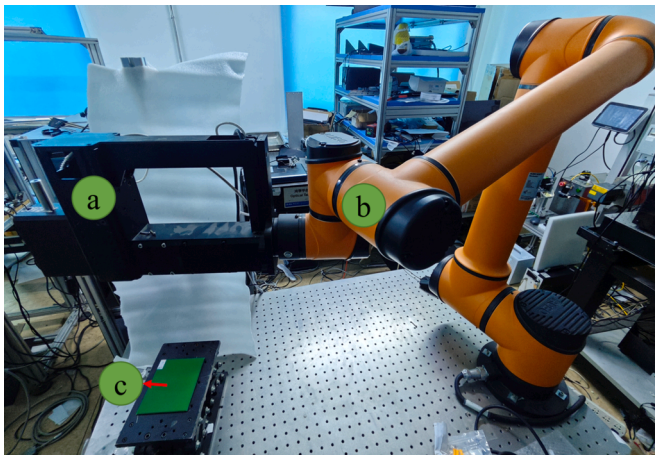


Fig. 3. Complete all-optical optical-acoustic fusion detection system. (a) Detection module, (b) robotic arm, (c) specimen.

(b) Laser head. A pulse laser (model PD-532–0.5-B) with a wavelength of 532 nm, pulse width of 1 μs, repetition rate of 1 kHz, and maximum single-pulse energy of 0.5 mJ, used for ultrasonic generation.

(c) Reflective mirror. An anti-reflection coated ZnSe plano-convex lens is employed to reflect visible light while transmitting infrared radiation, providing the optical foundation for the future integration of an optical–thermal–acoustic fusion detection system.

(d) Optical camera. Equipped with a BASLER acA2040-90 μm CMOS industrial camera (2048 × 2048 resolution), paired with a HN-2520–20 M−C1/1X fixed-focus lens (focal length 25 mm).

(e) Reserved port for IR camera (for future thermal imaging expansion).

Data acquisition is synchronized using a PCIe 69,834 high-speed data acquisition card, offering an 80 MHz sampling rate and 16-bit A/D resolution for high-fidelity capture of LUT signals from the F-P sensor.

After the camera's intrinsic matrix is obtained, the complete system workflow is summarized in Table 3.

The flowchart of the main work is shown in Fig. 5.

4. Results and discussion

4.1. Optical imaging

After system initialization, the detection module returns to its predefined working pose. The optical camera then captures an image of the specimen, as shown in Fig. 6.

The operator manually selects a target detection region through a rectangular selection on the graphical user interface. The system records the pixel coordinates of the corners in the target region, and these corner coordinates are transformed into precise world coordinates through the

Table 3
Step-by-step process of the optical-acoustic fusion detection system.

Step	Process Description
1	Initialize the detection module and set the predefined working pose of the detection module.
2	Move the detection module to the predefined working pose, place the calibration chessboard, and capture images.
3	Use the PnP algorithm to calculate the camera's extrinsic matrix.
4	Return the detection module to predefined working pose.
5	Place the specimen and acquire its optical image.
6	Select the target detection region in the optical image with the mouse box, and the software automatically records its coordinates.
7	Automatically move the detection module to the target detection region based on coordinate transformation and perform LUT.
8	Acquire LUT data, perform image registration and optical-acoustic fusion, and complete one detection cycle. Then return to Step 4.

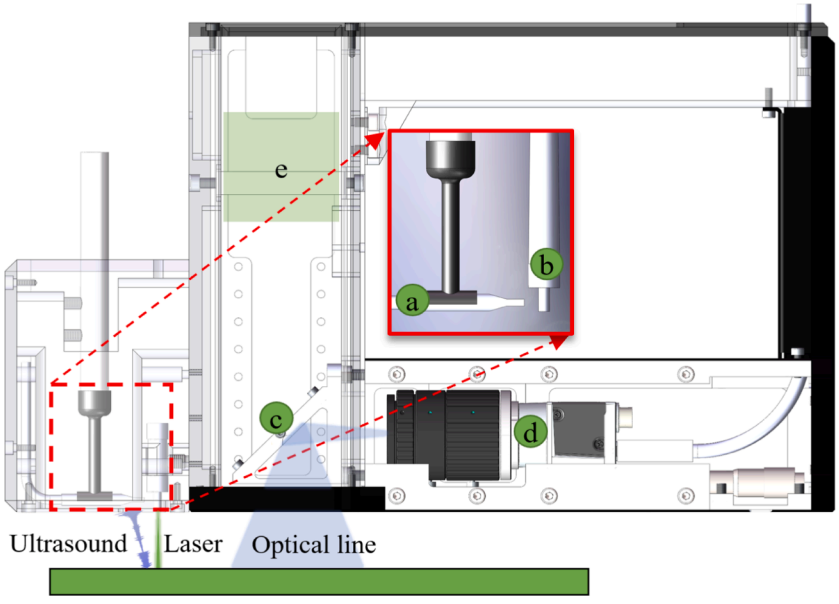


Fig. 4. Schematic of the detection module. (a) F-P acoustic sensor, (b) laser head, (c) reflective mirror, (d) optical camera, (e) reserved port for IR camera (for future thermal imaging expansion).

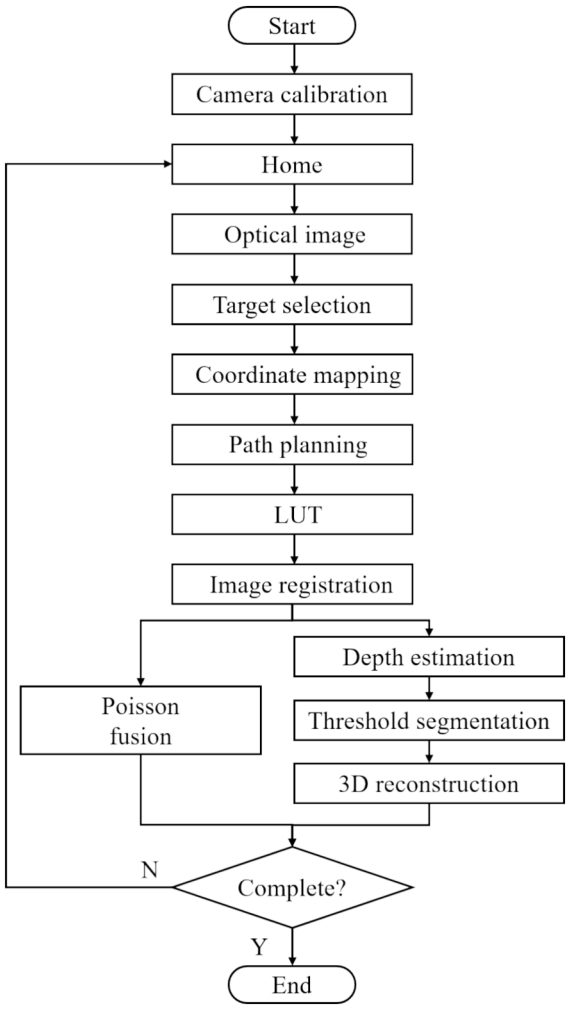


Fig. 5. The flowchart of the main work.

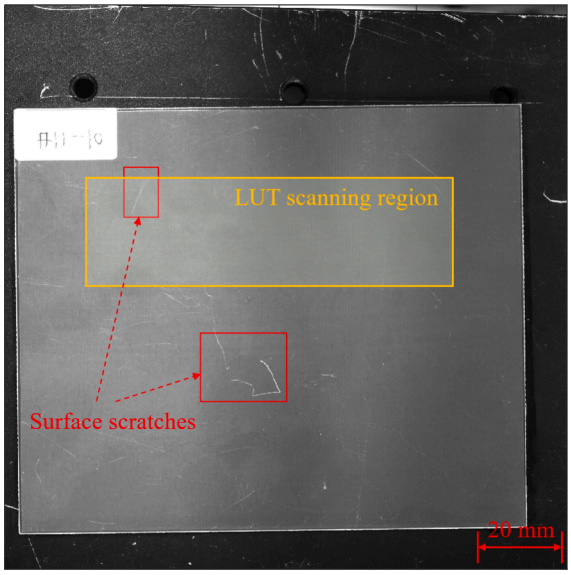


Fig. 6. Optical image with visible surface scratches, serving for target detection region selection and fusion benchmark.

established transformation. Based on this mapping, the robotic arm is commanded to automatically move the detection module to the target detection region.

Moreover, the acquired optical image reveals the presence of surface scratches and small defects. While such small surface defects may not be detected by LUT alone, they can be effectively visualized in the fusion images through the complementary coupling of optical and LUT features. This enhances the system's capability to identify surface defects.

4.2. LUT detection results

(1) Scanning parameters and detection process.

After completing the positioning of the target detection region, the system drives the 6-DOF robotic arm to automatically move the detection module to the starting position of the scan, based on the image-to-world coordinate transformation.

The scanning parameters are configured as follows: laser pulse energy is 0.5 mJ, scan step size is 0.2 mm, and scanning grid is 435 (x-direction) × 135 (y-direction), corresponding to a detection region of 87 mm × 27 mm. To reduce noise interference, each point is sampled 10 times and averaged to obtain valid acoustic data. In this experiment, the laser repetition rate is 1 kHz. 10 signals were collected at each measurement position (taking 10 ms), and combined with the movement time, the measured point acquisition rate was approximately 33 (points/s). It takes approximately 0.5 h to complete the overall scan.

(2) Feature extraction and imaging.

To extract defect-related information from the LUT data, principal component analysis (PCA) is employed for dimensionality reduction and image reconstruction, as detailed in Section 4.6. The PCA imaging results are shown in Fig. 7, PC1 primarily reflects the overall defect characteristics, while PC2 ~ PC6 contain residual defect characteristics that, although explaining minimal variance, contribute to defect boundary enhancement in the fusion image.

To enhance defect visibility and synthesize multi-component information, the L2-norm fusion method is applied to integrate the first six components into a single comprehensive LUT image, as shown in Fig. 8.

(3) Comparative analysis with IR.

As a commonly used method for defect detection, IR was employed as a benchmark for comparative evaluation in this study. The experiment was conducted on the same specimen to validate the performance advantages of the LUT method. This comparison is designed to assess the relative performance of the LUT method against IR under the specific experimental conditions. These findings pertain specifically to the experimental conditions of this study and do not constitute a general assessment of IR technology.

The IR system is shown in Fig. 9. The infrared camera used is the FLIR X6520SC, with a resolution of 640 × 512, thermal sensitivity of 20 mK, and a frequency of 50 Hz. A modulated halogen lamp serves as the thermal excitation source, with a power of 500 W, and the illumination uniformity on the specimen region is about 90 %. Lock-in method is used for defect imaging, the lock-in integration time is 50 s.

According to the theory of thermal diffusion, the thermal diffusion depth u is related to the modulation frequency f, which is described as:

$$\mu = \sqrt{\frac{\alpha}{\pi f}}, \alpha = \frac{k}{\rho c} \tag{4}$$

where α is the thermal diffusivity, k is the thermal conductivity, ρ is the material density, and c is the specific heat capacity. The physical parameters of FR4 are shown in Table 4.

Equation (12) shows that the modulation frequency is negatively correlated with the thermal diffusion depth. In lock-in method, the system needs to generate reference sine or cosine signals based on the preset excitation frequency, and divide each excitation cycle into several phase numbers according to the sampling frequency of the infrared camera. To ensure that each frame of image captured by the camera can be accurately aligned with a specific phase point of the reference signal, setting the number of camera sampling frames contained in each

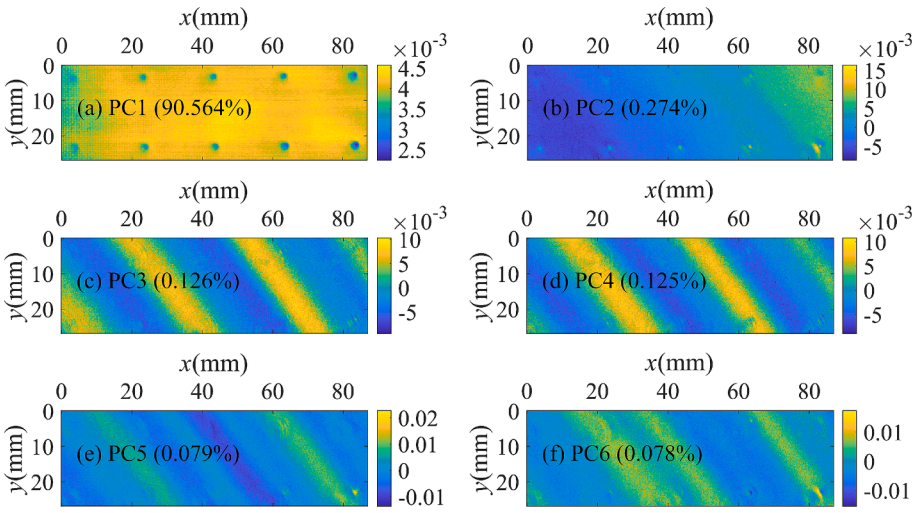


Fig. 7. Reconstructed images of the first six principal components (unit: a.u.). (a) PC1, variance 90.564 %, (b) PC2, variance 0.274 %, (c) PC3, variance 0.126 %, (d) PC4, variance 0.125 %, (e) PC5, variance 0.079 %, and (f) PC6, variance 0.078 %.

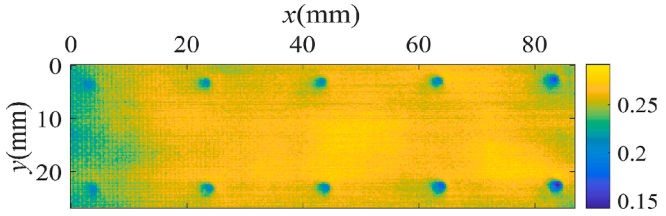


Fig. 8. LUT imaging result based on L2-norm fusion of PC1 ~ PC6 (unit: a.u.).

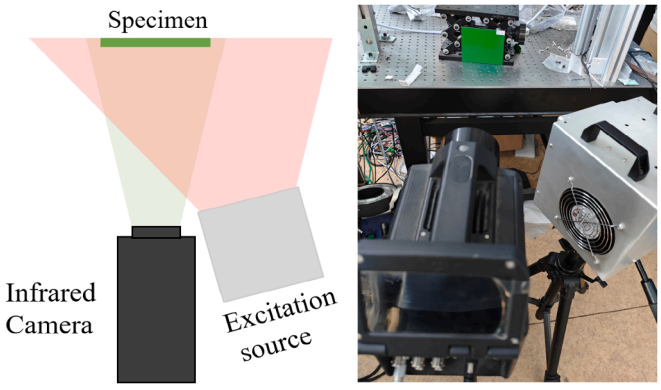


Fig. 9. Schematic diagram and equipment configuration of the IR detection system.

Table 4
Physical parameters of FR4.

Parameter	Value	Unit
Thermal conductivity	0.4	W/(m·K)
Density	1820	kg/m^3
Specific heat capacity	1100	J/(kg·K)

excitation cycle as an integer is a standard processing step.

Based on the expected defect depth range of 0.7 mm ~ 1.7 mm in this study, 4 typical modulation frequencies of 0.02 Hz, 0.05 Hz, 0.10 Hz, and 0.20 Hz were selected for the experiment. The theoretical thermal diffusion depth is 0.6 mm ~ 1.8 mm, which can ensure sufficient detection depth range while avoiding too long time caused by extremely low frequencies, and surface information dominance caused by extremely high frequencies. The resulting images are shown in Fig. 10, the color bar represents the lock-in amplitude signal intensity.

As observed from the IR results, the IR results obtained at excitation frequencies below 0.10 Hz appeared superior. Therefore, the result at 0.02 Hz, which exhibited the highest qualitative contrast among the set, was selected for the subsequent quantitative comparison with the LUT method. The detectable maximum depth-to-diameter ratio is used as an indicator of detection capability.

Under the experimental conditions of this study, the IR failed to identify defects #5, #8, #9, and #10 (SNR is recorded as 0), with depth-to-diameter ratios of 1.1333, 1.2005, 1.4000, and 1.7001, respectively. For this study, the detectable depth-to-diameter ratio for IR was below 1.1333. In comparison, the LUT method successfully detected all defects, with a maximum detectable depth-to-diameter ratio exceeding 1.7001. This suggests that, in the constraints of this experiment, the LUT method extended the detectable depth-to-diameter range considerably compared to the IR benchmark.

To quantitatively assess image quality, the average SNR of the image is given by:

$$SNR = \frac{\Delta S}{\sigma_N} \tag{5}$$

where ΔS is the absolute difference between the average values of the defect and background region, and σ_N is the standard deviation of the background region. The SNR of the LUT and IR imaging results is calculated as shown in Fig. 11. To enable a more accurate comparison of SNR between the IR and LUT methods, 3 independent and repeated trials were conducted for each method under identical experimental conditions. The means and standard deviations of all results are presented with error bars in Fig. 11.

The quantitative results show that the average SNR of the LUT image was 4.358, compared to 0.446 for the IR image. This indicates that the SNR of LUT is approximately 9.7 times higher than IR under these specific experimental conditions.

To ensure a relatively fair comparison, the IR and the LUT method were evaluated using the same PCB specimen. It should be noted that IR and LUT rely on fundamentally different physical mechanisms. This comparison proves that IR is effective for rapid large-area detection, whereas LUT provides higher sensitivity and suitable for precise detection of critical regions. Therefore, the purpose of this comparison is not to claim universal superiority of LUT over IR, but rather to highlight the advantages of the proposed method in subsurface defect positioning,

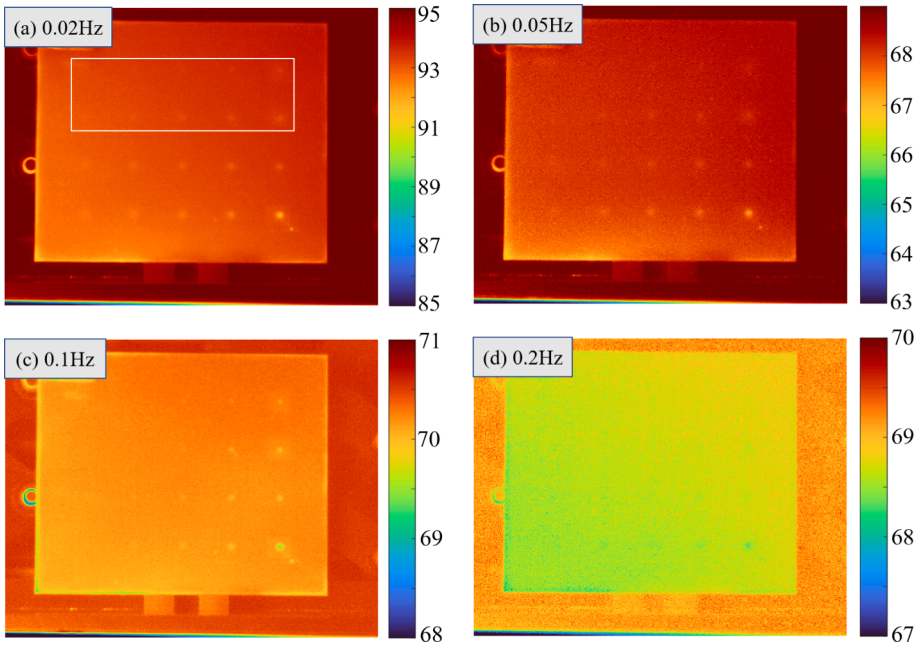


Fig. 10. IR results at different modulation frequencies (unit: a.u). (a) 0.02 Hz, (b) 0.05 Hz, (c) 0.1 Hz, (d) 0.2 Hz.

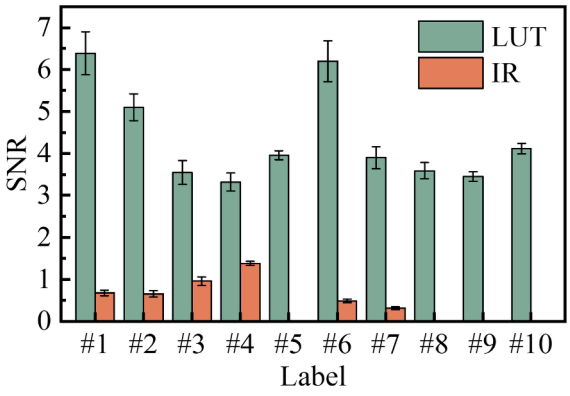


Fig. 11. Comparison of SNR values between LUT and IR results (mean ± standard deviation).

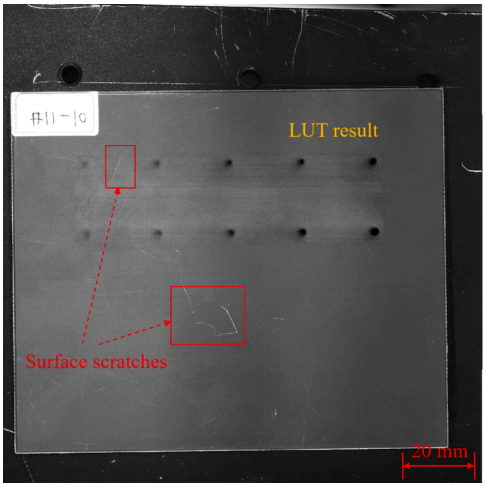


Fig. 12. Optical-acoustic fusion imaging result, combining surface optical features with subsurface LUT defect information.

spatial interpretability, and defect visualization.

Furthermore, IR and LUT should be regarded as complementary rather than mutually exclusive detection techniques. IR enables large-area rapid detection, while LUT is suited for high-resolution detection of critical regions. The fusion of these two methods can combine detection efficiency with high spatial resolution, and lays the foundation for future research on optical–thermal–acoustic multi-source data fusion.

4.3. *All-optical optical-acoustic fusion imaging*

After completing LUT detection and positioning of the target region in the world coordinate system, the system registers the LUT data with the corresponding optical image based on this positioning information. After successful registration, Poisson fusion was employed for pixel-level image fusion between LUT data and optical images to generate the final optical-acoustic fusion image, as shown in Fig. 12. The fusion image simultaneously displays surface morphology and subsurface defect features, facilitating intuitive observation of the spatial distribution of defects.

To evaluate the positioning accuracy of defects in the optical-acoustic fusion image, the optical image of the defect side was selected as the reference for the “true defect location.” A perspective transformation was applied to flatten and align the optical-acoustic fusion image with the reference image. On this basis, we unify the two images into the same coordinate system and calculated the corresponding error of the defect position. The reference image's transparency was set to 50 % for visual comparison, as shown in Fig. 13. The defect locations in the optical-acoustic fusion image closely match those in the reference image, demonstrating high positioning accuracy.

The positioning for defects #1 to #10 were quantified based on 3 independent trials. The means and standard deviations of all results are presented with error bars in Fig. 14. The overall root mean square (RMS) error is 0.32 mm, which confirms the high positioning accuracy of the proposed optical-based positioning method.

4.4. *Defect depth estimation*

Fig. 15 shows the representative LUT signals acquired from both defect-free and defect regions. For the specimen in this study, the

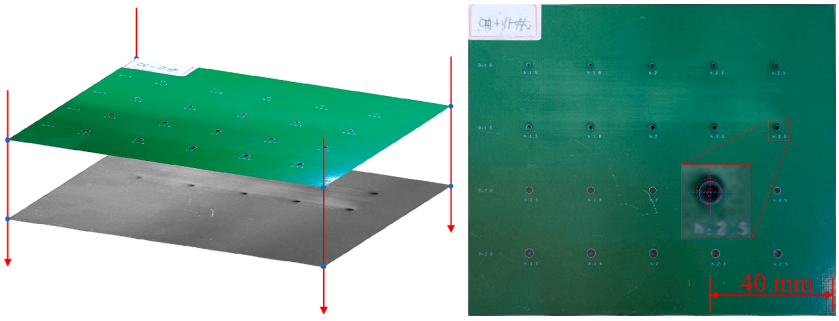


Fig. 13. Overlay of optical-acoustic fusion image and reference image from the defect side (reference image transparency set to 50 %).

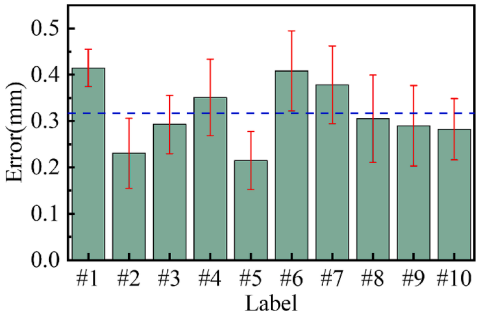


Fig. 14. Positioning errors of defects #1–#10.

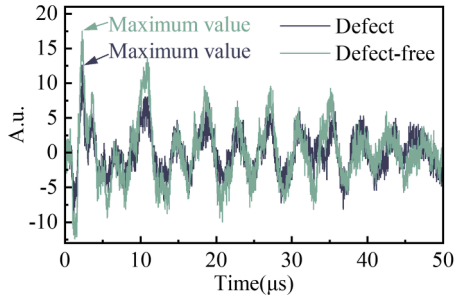


Fig. 15. LUT signals acquired from both defect and defect-free regions.

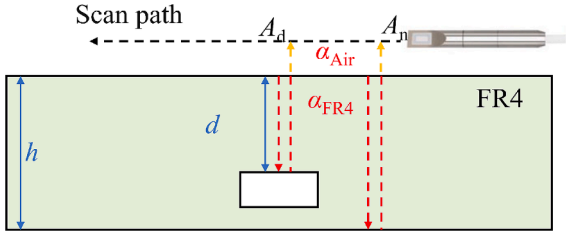


Fig. 16. Schematic diagram of defect depth calculation model based on acoustic attenuation law.

ultrasonic signals acquired by the F-P sensor exhibit complex time-domain structures, with very small time-of-flight (TOF) differences between defect and defect-free regions. This makes it challenging to estimate defect depth using conventional TOF-based approaches. In contrast, the signal amplitude demonstrates a more noticeable difference. Signals acquired from defect regions show stronger attenuation. Therefore, this study focuses on using acoustic attenuation to estimate defect depth.

When ultrasonic waves propagate in materials, ultrasonic energy attenuation is significantly influenced by the intrinsic properties of the

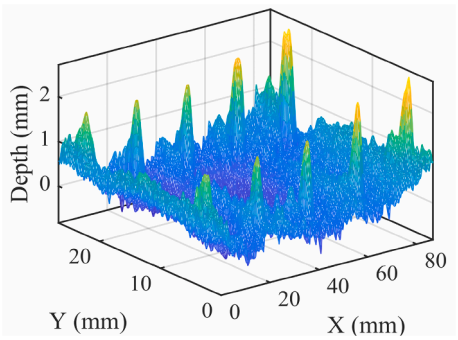


Fig. 17. Depth information ($h - d$) of each defect calculated based on the acoustic attenuation.

medium. Due to the big difference in acoustic impedance between the specimen material (FR4) and the defect (air), according to the relationship between reflectivity and acoustic impedance, approximately 99 % of the acoustic energy is reflected at the FR4-air interface. Therefore, the transmission and loss of the signal are ignored, the simplified acoustic attenuation model established in this study is illustrated in Fig. 16.

Based on a simplified attenuation assumption, the signal amplitude attenuates exponentially with propagation distance. Based on this principle, the following relationship is derived:

$$\frac{A_d}{A_n} = e^{2\alpha_{FR4}(h-d)} \tag{6}$$

where A_d is the ultrasonic signal amplitude measured at the defect region, A_n is the signal amplitude at a defect-free region, h is the thickness of the specimen, d represents the actual defect depth. Considering that LUT signals are essentially broadband and attenuation coefficient is frequency dependent, α_{FR4} in this study is the equivalent attenuation coefficient of material. It is treated as a constant to be calibrated.

In this study, the signal amplitudes A_d and A_n are taken as the peak values of the ultrasonic signal envelopes detected by the F-P acoustic sensor. To solve for unknown depth d, the model requires an estimation of α_{FR4}, which can be inferred based on known depth defects in the same material. For inhomogeneous materials, a multi-point calibration should be adopted to account for spatial variations of attenuation property.

To enable quantitative evaluation of defect depth dimensions, the depth information ($h - d$) of each defect was calculated based on the acoustic attenuation model. The results are illustrated in Fig. 17.

To assess the accuracy of the proposed depth estimation method, all defects within the LUT region were selected for quantitative analysis. The identical depth estimation method was adopted for the results of 3 independent repeated LUT experiments, and the mean estimated depths and their standard deviations (error bar) were compared with the actual defect values, as shown in Fig. 18.

The results indicate that the defect depth calculated by the acoustic

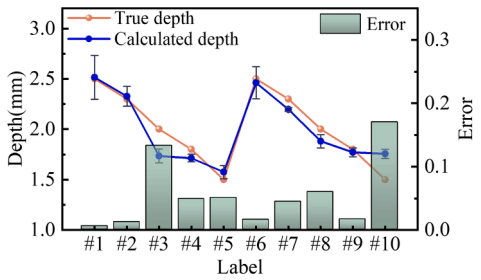


Fig. 18. Calculated depth information ($h - d$) and error value of each defect.

attenuation method is close to the actual defect depth. For the LUT detection region in this study, the minimum relative error is 0.55 %, the maximum relative error is 17.02 %, and the average relative error for all defects is 5.56 %. These results demonstrate the feasibility of the proposed attenuation-based approach for quantitative depth estimation. The main reasons for errors are as follows:

(1) **Ultrasonic propagation trajectory**. The lateral offset between the laser spot and the sensor leads to a tilted acoustic path, which our simplified attenuation model does not account for.

(2) **Random noise**. Inherent system and environmental noise perturb the laser-induced ultrasonic signal.

(3) **Loss and scattering**. Energy loss and scattering at interfaces (e.g., FR4-air) is ignored in the simplified attenuation model.

(4) **Material inhomogeneity**. Slight spatial variations in the PCB's density and stiffness affect local sound speed and attenuation.

In addition, for real defects, irregular geometries will introduce additional scattering errors. Future work could employ wavenumber-domain techniques to isolate direct reflections from complex scattered waves, and on the other hand, implement multi-point calibration instead of a single fixed attenuation parameter to better compensate for inhomogeneity materials or different structures (e.g., with copper traces, multilayer boards), thereby enhancing overall robustness.

4.5. 3D reconstruction of defects

Once the defect locations and corresponding depth values were obtained, 3D reconstruction of subsurface defects was performed to more intuitively understand the spatial characteristics of defects in material. To enhance the accuracy and clarity of the reconstruction, the threshold segmentation technique was applied to the depth map in order to remove background noise and defect-free regions. The segmented defect regions are illustrated in Fig. 19. To further evaluate the morphological fidelity of the reconstructed defect regions, the Intersection over Union (IoU) metric was introduced for quantitative assessment. The overall IoU value was calculated to be 0.643, indicating satisfactory geometric consistency and boundary reconstruction capability of the detected defects.

Based on the known geometric dimensions of the specimen, and calculated defect location and depth, a 3D model of the defects was constructed. The final reconstruction result is shown in Fig. 20. The reconstructed model clearly displays the surface morphology and subsurface defect characteristics of the material, including their size, shape, position, and depth.

To quantitatively evaluate the accuracy of 3D reconstruction, this study uses defect volume as the core indicator. Fig. 21 compares the calculated and actual values of each defect volume and the relative error. The results indicate that the reconstructed volumes of most defects are close to the actual values. The overall average relative error of all defect volume reconstruction results is 51.3 %.

Although some defects show relatively large volumetric errors, the reconstructed volumes show a consistent trend with the true values (linear correlation coefficient $R^2 = 0.865$), indicating that the proposed method provides a feasible approach for 3D reconstruction of materials.

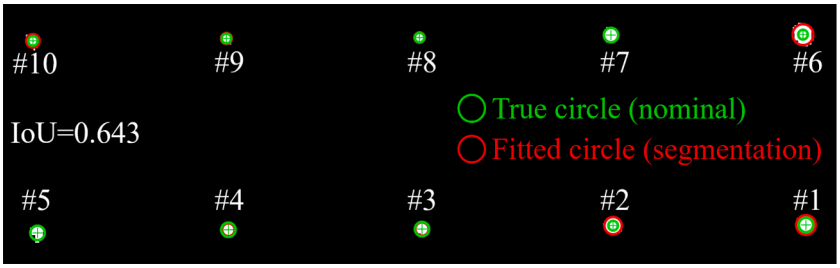


Fig. 19. Defect regions extracted by threshold segmentation. Circular annotations corresponding to the nominal defect diameters are overlaid on the segmented regions to facilitate visual assessment of shape fidelity.

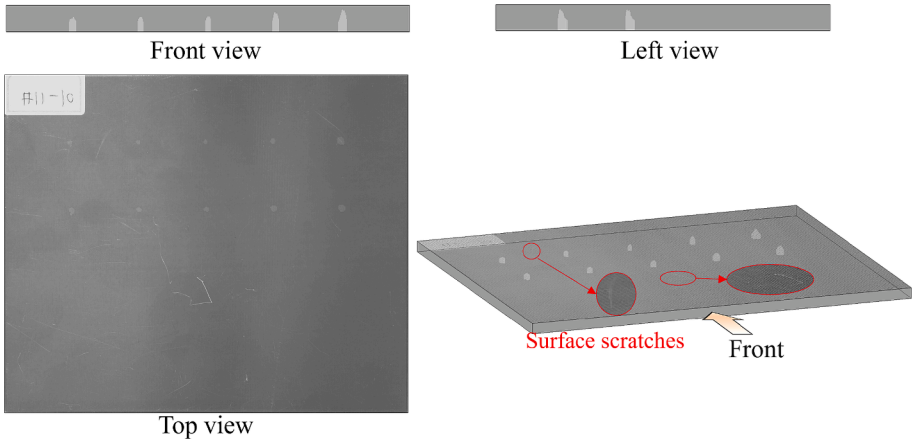


Fig. 20. 3D reconstruction results, fusing surface morphology and subsurface defect information.

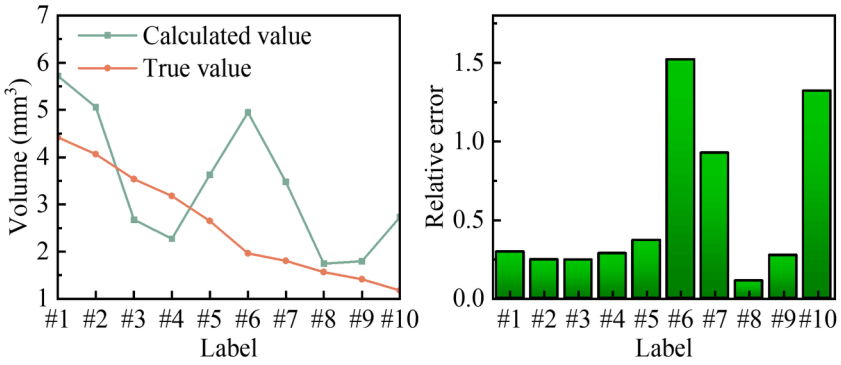


Fig. 21. Comparison and error of defect volumes in 3D reconstruction.

The primary source of volumetric error stems from uncertainties in both defect boundaries and depth estimates, which are amplified during the volume calculation process. Advanced segmentation and acoustic inversion models considering wave scattering will be explored to improve accuracy in future work.

4.6. Algorithmic details

PCA was applied for feature extraction. A minimum cumulative variance threshold of 90 % was adopted to ensure sufficient information retention. Although PC1 explains over 90 % of the total variance, higher-order components may still preserve limited defect-related information. Accordingly, on the basis of satisfying the 90 % threshold, 5 additional higher-order components were retained in this study. The imaging results remain stable when the number of retained components varies slightly, indicating low sensitivity to the exact choice of component number.

Poisson fusion was adopted for its ability to perform seamless, gradient-aware blending. Additional advantages include its stability, easy to implement, and lack of tunable parameters. The same fusion configuration was applied to all experiments without case-specific tuning and ensuring reproducibility.

In summary, Poisson fusion and PCA are deterministic and training-free methods that require no parameter tuning, making them stable, reproducible, and easy to implement.

5. Conclusions

This study proposed and validated an automated all-optical optical-acoustic fusion detection method. The core contribution is a system that spans from automated LUT scan planning to optical-acoustic data fusion and 3D defect visualization.

Under the experimental conditions of this study, compared to IR, the LUT method demonstrates superior performance, the image SNR improved by approximately 9.7 times, and the maximum detectable depth-to-diameter ratio increased by over 50 %. Positioning errors remained RMS < 0.32 mm, and depth estimation through an acoustic attenuation model yielded an average relative error of 5.56 %, and the IoU for 2D shape fidelity was approximately 0.643. Furthermore, a preliminary 3D reconstruction capability was demonstrated, effectively visualizing defect geometry, and the overall average relative error of all defect volume reconstruction results is 51.3 %, $R^2 = 0.865$, validating the feasibility of the proposed method.

In conclusion, this work validates the feasibility of proposed all-optical optical-acoustic fusion method for automating defect detection and enhancing visualization. Future work will focus on improving the robustness for complex defect geometries, integrating IR to enhance detection efficiency, and conducting detection experiments for actual PCB defects in industrial components.

CRediT authorship contribution statement

Jianghao Zhao: Writing – original draft. **Fei Wang:** Conceptualization. **Peng Yin:** Data curation. **Zhuoyan Yue:** Formal analysis. **Feng Yang:** Methodology. **Honghao Yue:** Project administration. **Stefano Sfarra:** Investigation. **Lixia Xu:** Investigation. **Xiaqiao Li:** Validation. **Dongkangkang Chen:** Visualization. **Junyan Liu:** Writing – review & editing.

Declaration of competing interest

The authors declare that they have no known competing financial interests or personal relationships that could have appeared to influence the work reported in this paper.

Acknowledgments

This work was supported by the National Natural Science Foundation of China (No. U2570237, No. 62201173), the National Natural Science Foundation of China under the Basic Science Center Program for “Space Robot Intelligent Manipulation” (Grant No. T2388101), Postdoctoral innovative talents support program (No. BX2021092), fundamental research funds for the central universities (2023FRFK02046), Foreign expert exchange program of HIT (No. D20240030) and the Programme of Introducing Talents of Discipline of Universities (Grant No. B07108), State Key Laboratory of Robotics and System (HIT),JSZL (JSZL2020204A002).

Data availability

Data will be made available on request.

References

[1] F. Wang *et al.*, “Laser-induced thermography: An effective detection approach for multiple-type defects of printed circuit boards (PCBs) multilayer complex structure,” *Measurement*, vol. 206, Jan. 2023, Art. no. 112307.
[2] Y. Zhou, et al., Review of vision-based defect detection research and its perspectives for printed circuit board, J. Manuf. Syst. 70 (Oct. 2023) 557–578.
[3] D. T. Dumpert, “Infrared techniques for printed circuit board (PCB) evaluation,” in *Infrared Methodology and Technology*, Boca Raton, FL, USA: CRC Press, 2023, pp. 253–264.
[4] Z. Wang, et al., Anomaly detection and fault classification of printed circuit boards based on multimodal features of infrared thermal imaging, IEEE Trans. Instrum. Meas. 73 (2024) 1–13.
[5] A. Stoynova, B. Bonev, and N. Brayanov, “Thermographic approach for reliability estimation of PCB,” in *Proc. 41st Int. Spring Semin. Electron. Technol*, 2018, pp. 1–7.
[6] I. Alqurashi, N. Alver, U. Bagci, F.N. Catbas, A review of ultrasonic testing and evaluation methods with applications in civil NDT/E, J. Nondestruct. Eval. 44 (2) (2025) 1–34.
[7] V. Tinard, C. Fond, and P. Francois, “Eliminating the effect of couplant on ultrasonic characterisation of solids: Experimental and theoretical investigations,” *NDT & E Int.*, vol. 154, 2025, Art. no. 103385.
[8] F. Bertocci, A. Grandoni, and T. Djuric-Rissner, “Scanning acoustic microscopy (SAM): A robust method for defect detection during the manufacturing process of

ultrasound probes for medical imaging," *Sensors*, vol. 19, no. 22, 2019, Art. no. 4868.
[9] M. I. Silva *et al.,* "Review of conventional and advanced non-destructive testing techniques for detection and characterization of small-scale defects," *Prog. Mater. Sci.*, vol. 138, 2023, Art. no. 101155.
[10] M. Strąg and W. Swiderski, "Defect detection in aramid fiber-reinforced composites via terahertz radiation," *J. Nondestruct. Eval.*, vol. 42, no. 1, 2023, Art. no. 9.
[11] S. Everton, P. Dickens, C. Tuck, and B. Dutton, "Evaluation of laser ultrasonic testing for inspection of metal additive manufacturing," in *Proc. Laser 3D Manuf. II*, vol. 9353, Mar. 2015, pp. 145–152.
[12] L. Xie, Y. Lian, F. Du, Y. Wang, and Z. Lu, "Optical methods of laser ultrasonic testing technology in industrial and engineering applications: A review," *Opt. Laser Technol.*, vol. 176, 2024, Art. no. 110876.
[13] X. Kou, C. Pei, and Z. Chen, "Fully noncontact inspection of closed surface crack with nonlinear laser ultrasonic testing method," *Ultrasonics*, vol. 114, 2021, Art. no. 106426.
[14] A. Zarei and S. Pilla, "Laser ultrasonics for nondestructive testing of composite materials and structures: A review," *Ultrasonics*, vol. 136, 2024, Art. no. 107163.
[15] L. Xu *et al.,* "Application of laser ultrasonic testing technology in the inspection of cabin structures," *J. Phys.: Conf. Ser.*, vol. 3026, no. 1, Jun. 2025, Art. no. 012044.
[16] A. Poole, M. Sutcliffe, G. Pierce, et al., Autonomous, digital-twin free path planning and deployment for robotic NDT: introducing LPAS: locate, plan, approach, scan using low cost vision sensors[J], Appl. Sci. 12 (10) (2022) 5288.
[17] Wang P, Dong X, Yang Y, et al. Robot-Assisted Trajectory Planning Method for NDT [C]//2023 IEEE 6th International Conference on Industrial Cyber-Physical Systems (ICPS). IEEE, 2023: 1-6.
[18] K.S. Ma, K.J. Lee, J.R. Lee, A study on 3D scan-based robot arm control approach for pulse-echo laser ultrasonic testing of curved composite structures[J], Meas. Sci. Technol. 36 (4) (2025) 045903.
[19] K.J. Lee, J.R. Lee, Path planning and inspection of complex-shaped 3D-printed composites based on robotic pulse-echo laser ultrasonic testing[J], Adv. Compos. Mater 34 (2) (2025) 329–351.
[20] J. Park, J. Ahn, S. Ban, et al., Multicontrast and nondestructive transparent ultrasound transducer-based photoacoustic and optical coherence imaging of multilayered electronics[J], IEEE Trans. Instrum. Meas. 73 (2024) 1–9.
[21] Z. Chen, Q. Zhang, M. Zhong, et al., Multidimensional computed measurement for highly accurate PCBA defect detection[J], Opt. Express 33 (3) (2025) 5340–5354.
[22] J. Park, J. Ahn, and C. Kim, "Non-destructive quality testing with photoacoustic imaging and optical coherence tomography," in *Proc. High-Power Laser Mater. Process.: Appl., Diagn., Syst. XIII*, vol. 12878, 2024, pp. 127–131.
[23] S. Li, et al., Pixel-level image fusion: a survey of the state of the art, Inf. Fusion 33 (2017) 100–112.
[24] Z. Chen, et al., Multidimensional computed measurement for highly accurate PCBA defect detection, Opt. Express 33 (3) (2025) 5340–5354.
[25] Queiroz R S, Silva J P B, das Neves E C, et al. Development and fusion of NDT classifiers for defect detection on underwater structures[J]. NDT & E International, 2024, 144: 103098.
[26] W. Xu, X. Li, J. Zhang, Multi-feature fusion imaging via machine learning for laser ultrasonic based defect detection in selective laser melting part[J], Opt. Laser Technol. 150 (2022) 107918.
[27] H. Zhang, H. Xu, X. Tian, et al., Image fusion meets deep learning: a survey and perspective[J], Inf. Fusion 76 (2021) 323–336.
[28] P. Song, et al., Contactless inspection of CFRP artificial disbonds using combined laser thermography and laser ultrasonics with optical microphone, Compos. Struct. 33 (2022).
[29] G. Wissmeyer *et al.,* "Looking at sound: Optoacoustics with all-optical ultrasound detection," *Light Sci. Appl.*, vol. 7, no. 1, 2018, Art. no. 53.
[30] J. Chen, et al., Micro-fiber-optic acoustic sensor based on high-Q resonance effect using Fabry–Pérot etalon, Opt. Express 29 (11) (2021) 16447–16454.
[31] Y. Wang, et al., A comprehensive study of optical fiber acoustic sensing, IEEE Access 7 (2019) 85821–85837.
[32] T. Li, et al., Recent progress in fiber optic acoustic sensor and its applications: a review, IEEE Sens. J. (2024).
[33] Z. Zhang, A flexible new technique for camera calibration, IEEE Trans. Pattern Anal. Mach. Intell. 22 (11) (2002) 1330–1334.